

This is the accepted manuscript made available via CHORUS. The article has been published as:

Charge-Collection Efficiency in Back-Illuminated Charge-Coupled Devices

Guillermo Fernandez Moroni, Kevin Andersson, Ana Botti, Juan Estrada, Dario Rodrigues, and Javier Tiffenberg

Phys. Rev. Applied **15**, 064026 — Published 10 June 2021

DOI: [10.1103/PhysRevApplied.15.064026](https://doi.org/10.1103/PhysRevApplied.15.064026)

Charge collection efficiency in back-illuminated Charge-Coupled Devices.

Guillermo Fernandez Moroni,^{1,*} Kevin Andersson,^{2,1,†} Ana Botti,^{2,‡}
 Juan Estrada,^{1,§} Dario Rodrigues,^{2,1,¶} and Javier Tiffenberg^{1,**}

¹*Fermi National Accelerator Laboratory, PO Box 500, Batavia IL, 60510, USA*

²*Department of Physics, FCEN, University of Buenos Aires and IFIBA, CONICET, Buenos Aires, Argentina*

(Dated: May 20, 2021)

Low noise fully-depleted Charged Coupled Devices have been identified as a unique tool for dark matter searches, low energy neutrino physics, and X-ray detection. The charge collection efficiency (CCE) for these detectors is a critical performance parameter for current and future experiments. We present a technique to characterize the CCE in back-illuminated CCDs based on soft X-rays. This technique is used to study two different detector designs. The results demonstrate the importance of the backside processing for the detection of charge packages near threshold, showing that a recombination layer of a few microns significantly distorts the low energy spectrum. The studies demonstrate that the region of partial charge collection can be reduced to less than 1 μm thickness with adequate backside processing.

I. THICK FULLY DEPLETED CCDS FOR DARK MATTER, NEUTRINO EXPERIMENTS, AND X-RAY DETECTION

Charged Coupled Devices (CCD) with low readout noise and large active volume have been identified among the most promising detector technologies for the low-mass direct dark matter search experiments, probing electron and nuclear recoils from sub-GeV DM [1–5]. The recent development of the Skipper-CCD [6, 7] demonstrated the ability to measure ionization events with sub-electron noise extending the reach of this technology to unprecedented low energies. Experiments based on this technology are planned for the coming years with active masses going from 100 grams to several kilograms [8, 9]. At the same time, the low noise CCD technology has been implemented in low energy neutrino experiments [10, 11] and are planned for future developments [12]. Back-illuminated CCDs are also broadly used as soft X-rays detectors in space-based X-ray telescopes [13–16] and ground-based instruments associated with advanced light sources [17].

There are several key performance parameters for the CCD sensors to be used in future instruments that are part of a significant R&D effort for future projects [8, 9, 12]. The most important performance requirements are the pixel dark current [7], readout noise optimization [18], and charge transport in the sensor [19].

The Charge Collection Efficiency (CCE) is defined as the fraction of the total charge produced during an ionization event that is collected in the CCD pixel for later readout.

The electric field required to fully deplete a silicon volume is related to the dopant concentration and temperature of the sensor [20]. When the strength of the electric field is not enough to reach this condition, recombination can occur as the electron-hole pair lifetime becomes smaller than the amount of time that it spends on the undepleted region [21]. While geminate recombination can occur at any applied voltage, this effect is beyond the scope of this paper, and does not affect the results.

In the back side of CCDs the dopant concentration can be non-uniform and have a large gradient [20]. In the active volume of a fully depleted detector, CCE is approximately 100% but in regions with higher dopant concentration the reduced mobility, lifetime, and local electric field experienced by the charge carriers can lead to recombination [22]. In these regions CCE could be less than 100%. The quantitative measurement of this effect is the goal of this work. Regions of partial CCE distort the measured spectrum of ionization events, affecting energy calibration and particle identification.

Back-illuminated CCDs in astronomy are treated to have a thin entrance window for light, with low reflectivity. This is especially important when detectors are used for wavelength shorter than 500 nm [23–25]. The measurements presented in Ref.[26] compare the detection efficiency for visible photons with the reflectivity. These studies show that all photons with wavelengths (absorption lengths) between 650 nm (3.6 μm) and 850 nm (18.7 μm) are fully detected unless they are reflected on the back surface. These results suggest that the bulk of the detector has 100% CCE, and that any recombination on these sensors occurs only on the first few microns near the back surface.

For thick CCDs, as those used in dark matter [1–7] and neutrino experiments [10, 11], a backside ohmic contact is required to apply the needed substrate bias to fully deplete the sensor [20]. At the same time, different processing techniques are used on the backside to reduce dark current. The backside processing of these sensors determines the field shaping near the surface and has a

* gfmoroni@fnal.gov

† kevinandersson456@gmail.com

‡ abotti@df.uba.ar

§ estrada@fnal.gov

¶ rodriguesfm@df.uba.ar

** javiert@fnal.gov

large impact on the CCE for events in that region. We study here the CCE for back-illuminated detectors with more than 200 μm thickness.

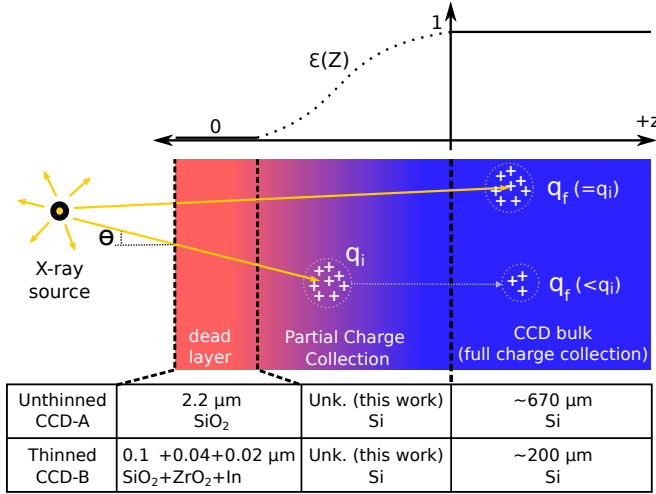


FIG. 1. Sketch of the CCD back illumination with an X-ray source. The photon penetrates the CCD producing a cloud of charge q_i , the fraction $\varepsilon(z)$ of this charge that is collected depends on the depth z . The region near the back of the CCD where $0 < \varepsilon(z) < 1$ is the PCC layer. The shape of $\varepsilon(z)$ is arbitrary for purposes of illustration.

II. DETERMINATION OF THE BACKSIDE CCE USING X-RAYS

X-rays can be used to characterize the CCE near the back surface of a CCD. In Fig. 1 we provide a schematic view of our X-ray experimental setup together with the critical variables used in this analysis. Below we list important aspects and definitions used in this work:

- The X-ray source was placed facing the back side of the device. Photons reaching the sensor are broadly distributed in a big area of the array. The geometry of the source and relative position to the device determine the incident angle of the X-ray. We call $h(\theta)$ to the probability density function (*pdf*) of possible incident angles θ of photons in the region of interest in the detector (with θ the angle between the sensor normal and the photon as depicted in Fig. 1). $h(\theta)$ can be evaluated numerically using a simple toy Monte Carlo simulation that reflects the geometry of the experimental setup. This toy-MC doesn't simulate particle interactions as its goal is to provide the intensity and incidence angle of the X-rays. We compared the $h(\theta)$ obtained this way with another obtained from a detailed Geant4 simulation (see Sec. III A) and found excellent agreement between them.
- The X-ray photons can reach the PCC layer and the bulk of the sensor volume. They will mainly inter-

act by photoelectric absorption following an exponential distribution in the amount of material traversed. The depth of the interaction in the silicon also depends on the incident angle θ . The joint *pdf* governing the incident angle and depth of interaction is $g'(z, \theta) = \exp(-z/(\lambda \cos(\theta)))h(\theta)/(\lambda \cos(\theta))$ for $z \geq 0$ ($g'(z, \theta) = 0$ for $z < 0$), where z is the depth in the silicon measured from the back of the sensor, λ is the attenuation length of the photon. The sensor position relative to the source defines the expected maximum and minimum incident angles (θ_1 and θ_2 , respectively) of the photons. These limits are used to calculate the marginal *pdf* of the interaction depth in the sensor.

$$g(z) = \int_{\theta_1}^{\theta_2} g'(z, \theta) d\theta. \quad (1)$$

- X-rays produce ionization events with a charge mean value $q_i = E_i/\epsilon$, where E_i is the energy of the photon and $\epsilon = 3.75 \text{ eV}$ is the mean ionizing energy [27]. We assume that the initial charge packet for all photoelectric absorption events is given by a Gaussian distribution with a mean equal to the X-ray energy and a width given by the Fano fluctuations [27]. The primary charge ionization is the same for the PCC layer and the bulk of the sensor as represented in Fig. 1.
- $\varepsilon(z)$ is the CCE function in the backside of the detector. The function indicates the fraction of carriers that are collected by the pixel after drifting away from the PCC layer (carriers that do not recombine in the PCC layer). This function depends on the depth of the interaction. If the primary interaction occurs closer to the back of the CCD (further away from the bulk of the sensor), carriers will have more options to recombine before they reach the bulk. Thus, $\varepsilon(z)$ increases monotonically.
- q_f is the charge that escapes from the PCC layer and can be collected and recorded by the sensor. As illustrated in Fig. 1, this will depend on the interaction depth of the photon. The *pdf* governing the distribution of possible values of q_f is called $f(q_f)$, which is the measurable differential spectrum from the output images of the detector. This distribution includes the fluctuations that are produced by the readout noise of the detector, typically Gaussian for scientific CCDs [21].

From the previous definitions, the measured charge can be expressed as

$$q_f = q_i \varepsilon(z). \quad (2)$$

where the measured charge q_f is a function of the produced charge, q_i , and the charge production depth, z . For events that are produced deep in the CCD, $\varepsilon = 1$ and $q_f = q_i$ (Fig. 1).

A. Determination of the efficiency function using a monochromatic X-ray source

From Eq. (2) and due to the monotonically increasing $\varepsilon(z)$ there is a one-to-one relationship between the final collected charge of a photon and its interaction depth in the PCC layer for the case of a mono-energetic X-ray source. Any measured event with charge packet smaller than q_i carries information of the efficiency function. Then, there is a one-to-one relationship between the cumulative distribution function (*cdf*) of the measured spectrum ($F(q_f)$) and the *cdf* of the interaction depth ($G(z)$)

$$F(q_f) = \int_0^{q_f} f(x)dx = \int_0^z g(x)dx = G(z) \quad (3)$$

where $f(x)$ is the measured spectrum and z is such that $\varepsilon(z) = q_f/q_i$.

Because the measurements at low charge values can be affected by readout noise it is experimentally useful to use the complement of the *cdf*: integrating from the energy of the X-ray peak in the direction of low charge values. This reduces the systematic uncertainties related to the modeling of the readout noise at low signal levels. In this case, Eq. 3 can be rewritten as

$$1 - F(q_f) = \int_{q_f}^{q_i} f(x)dx = \int_z^\infty g(x)dx = 1 - G(z) \quad (4)$$

Then the method consists of finding z for each q_f such that $1 - G(z) = 1 - F(q_f)$. Then for each (z, q_f) pair the efficiency function is $\varepsilon(z) = q_f/q_i$.

The method to calculate the CCE using a monochromatic X-ray peak is summarized in Table II of the Appendix. Partial charge depositions by secondary low probability X-ray interaction in the bulk of the sensor could add systematic errors to the previous method. Its contribution depends on the setup geometry and sensor dimensions and materials. In section III we discuss the impact of these effects using a detailed Geant4 simulation.

It is also possible to work directly with the *pdf* instead of the *cdf* but this approach is numerically harder and requires assumptions on the shape of $\varepsilon(z)$ to be solvable.

B. Determination of the efficiency function using an ^{55}Fe source

^{55}Fe X-ray sources are broadly used in the calibration of CCDs and for the characterization of their performance [21]. In this article, we extend its use to the characterization of the CCE in the PCC layer using the methodology proposed in Section II A. The main characteristics of the X-rays emitted by ^{55}Fe are summarized in Table I. The two K_α lines have similar energy and attenuation length and can be treated as a single monoenergetic X-ray line for this analysis.

In this case, the joint *pdfs* for the interaction depth ($z \geq 0$) and incident angle are

$$g'_\alpha(z, \theta) = \exp(-z/(\cos(\theta)\lambda_\alpha))h(\theta)/(\cos(\theta)\lambda_\alpha) \quad (5)$$

and

$$g'_\beta(z, \theta) = \exp(-z/(\cos(\theta)\lambda_\beta))h(\theta)/(\cos(\theta)\lambda_\beta) \quad (6)$$

for the X_{K_α} and X_{K_β} , respectively. λ_α and λ_β are the attenuation length for each photon from Table I. The angular distribution is the same in both cases. $g'_\alpha(z, \theta) = g'_\beta(z, \theta) = 0$ for $z < 0$.

The *cdf* of the measured spectrum can be expressed as

$$F(q_f) = p_\alpha F_\alpha(q_f) + p_\beta F_\beta(q_f), \quad (7)$$

F_α and F_β are the *cdfs* of the spectrum of events for each photon, and p_α and p_β are the relative intensities given in Table I normalized by the number of disintegrations. Generalizing Eq. 3

$$F_\alpha(q_f) = G_\alpha(z_\alpha) \text{ and } F_\beta(q_f) = G_\beta(z_\beta) \quad (8)$$

where G_α and G_β are the *cdfs* of the interaction depth of the X_{K_α} and X_{K_β} , respectively. They are obtained after integrating the *pdf* in Eq. 5 and 6 over all the possible values of θ (as in Eq. 1). z_α and z_β are interaction depths such that $\varepsilon(z_\alpha) = q_f/q_{i,\alpha}$ and $\varepsilon(z_\beta) = q_f/q_{i,\beta}$, where $q_{i,\beta}$ and $q_{i,\alpha}$ are the expected number of electron-hole pairs produced by the X_{K_α} and X_{K_β} photons from Table I. Since we assume a monotonically increasing $\varepsilon(z)$ function, then $z_\alpha \geq z_\beta$. Replacing Eq. 8 in 7

$$F(q_f) = p_\alpha G_\alpha(z_\alpha) + p_\beta G_\beta(z_\beta) \text{ with } z_\alpha \geq z_\beta. \quad (9)$$

A recursive nonlinear numeric solver can be used to find the z_α and z_β that solve this equation in an iterative way. We start with an ansatz for the CCE function, $\varepsilon_0(z)$, from which we obtain $z_{\beta,0}$ as a function of $z_{\alpha,0}$ using $q_f = q_{i,\alpha}\varepsilon_0(z_{\alpha,0}) = q_{i,\beta}\varepsilon_0(z_{\beta,0})$. Then, the right side of Eq. 9 can be rewritten as a function of $z_{\alpha,0}$ only, and numerically solved (as Eq. 4) to obtain an instance of the CCE function: $\varepsilon_1(z)$. Using $\varepsilon_1(z)$ as the ansatz this process can be repeated until the difference between the CCE function obtained from Eq. 9 and the ansatz is smaller than the required accuracy.

X_K	E [keV]	<e-h> prod. (q_i)	Rel. Int.	Att. lg. (λ)
α_2	5887.65	1570	0.297 (5)	28.7
α_1	5898.75	1573	0.583 (10)	28.9
β_3	6490.45	1731	0.120 (2)	38.0

TABLE I. ^{55}Fe X-rays energies, mean e-h pairs production (using the mean ionization energy), relative intensity, and attenuation length in μm [28].

Although the procedure described above is required to obtain the most precise measurement of $\varepsilon(z)$, three features of the ^{55}Fe source can be used to greatly simplify the problem when a $\sim 10\%$ error is acceptable:

- Larger number of K_α than K_β photons, since $p_\alpha/p_\beta = 7.33$,
- $G_\alpha(z_\alpha)$ and $G_\beta(z_\beta)$ are continuous and similar,
- $q_{i,\beta}$ and $q_{i,\alpha}$ differ only by 10%.

As the interactions in the PCC layer are dominated by the K_α photons (7.33 times more intense), only a small contribution is introduced by the photons from the K_β peak. The treatment of Eq. 9 can be greatly simplified by the approximation: $z_{\text{eff}} = z_\alpha = z_\beta$, where z_{eff} is an effective interaction depth value that will be between the true z_α and z_β . Under this approximation, a rough estimate of the error can be obtained by computing ε under two extreme assumptions for initial charge package:

1. $\varepsilon_{\text{high}}(z_{\text{eff}}) = q_f/q_{i,\alpha}$
2. $\varepsilon_{\text{low}}(z_{\text{eff}}) = q_f/q_{i,\beta}$

The difference between them is smaller than 10% and the true value for ε lies between these two extreme cases. If we use a more realistic effective value, q_{eff} , for the initial charge packet:

$$q_{\text{eff}} = p_\alpha q_{i,\alpha} + p_\beta q_{i,\beta} \quad (10)$$

the CCE function that is obtained is almost identical to the one resulting from the iterative "exact" solution of Eq. 9.

A summary of the proposed method to evaluate the PCC layer using an ^{55}Fe source is provided in Table III, in the Appendix.

III. EXPERIMENTAL RESULTS

We study here two CCDs with different backside treatments.

CCD-A was designed by the LBNL Microsystems Laboratory (MSL) [29] and fabricated at Teledyne-DALSA as part of the R&D effort for low energy neutrino experiments [10] and low mass direct dark matter search [3]. This is a rectangular CCD with 8 million square pixels of $15\text{ }\mu\text{m} \times 15\text{ }\mu\text{m}$ each. The CCD is fabricated in n-type substrate with a full thickness of $675\text{ }\mu\text{m}$. The resistivity of the substrate is greater than $10000\text{ }\Omega\text{-cm}$. The CCD is operated with a 40 V bias voltage that fully depletes the high-resistivity substrate using the method developed in Ref.[20]. To trap impurities that migrate during the sensor processing, a $1\text{ }\mu\text{m}$ thick in-situ doped polysilicon (ISDP) layer is deposited on the backside of the detector. This layer plays a critical role in controlling the dark current of the detector. Additional layers of silicon nitride, phosphorous-doped polysilicon, and silicon

dioxide are added to the backside ($2\text{ }\mu\text{m}$ total thickness). Phosphorous can migrate into the high resistivity material producing a region of a few microns where charge can recombine before drifting to the collecting gates of the detector. This region constitutes the PCC layer that we characterize with ^{55}Fe X-rays, as shown in Fig. 1.

CCD-B was also designed by the MSL and fabricated in high resistivity n-type silicon at Teledyne-DALSA using the same process as CCD-A with a few important differences: the detector has 4 million $15\text{ }\mu\text{m} \times 15\text{ }\mu\text{m}$ pixels, and a thickness of $200\text{ }\mu\text{m}$. The backside of the sensor was processed for astronomical imaging using a technique developed at the MSL [20] to improve the sensitivity to blue light. A backside ohmic contact is formed by low-pressure, chemical-vapor deposition ISDP. This layer is made thin, typically 10-20 nm, to minimize the absorption of blue photons and is robust to the over-depleted operation that is necessary to guarantee full depletion across the entire CCD. This detector is operated at a bias voltage of 40 V. Because of its backside treatment, this detector is not expected to have significant charge recombination near the back surface. The detector is exposed to ^{55}Fe X-rays on the backside, as shown in Fig. 1.

We used a standard ^{55}Fe calibration source encapsulated in stainless steel. Its active area is covered by a circular beryllium window 0.25 mm thick and 5 mm in diameter. The active ^{55}Fe foil is $1\text{ }\mu\text{m}$ thick and is deposited on a nickel backing. It was located 3.55 cm away from the CCDs. As the events produced in the PCC region may show a non-standard shape we did not use any quality cuts related to the shape of the events. To avoid edge-related effects, only events 50 pixels away from the edge of the sensor were considered in the analysis.

The effective depth distribution of interacting photons was calculated using a toy Monte Carlo simulation. After inspecting its functional form we found that it can be accurately parametrized by the sum of two independent exponential functions:

$$G(z) = \tilde{I}_\alpha * \exp(-z/\tilde{\tau}_\alpha) + \tilde{I}_\beta * \exp(-z/\tilde{\tau}_\beta), \quad (11)$$

where \tilde{I}_α (\tilde{I}_β) and $\tilde{\tau}_\alpha$ ($\tilde{\tau}_\beta$) are obtained by fitting the PDF produced from the MC simulation and represent the effective relative intensity and optical depth for the α (β) spectral line after the angular distribution of the photons is taken into account. For the geometry of our experimental setup we obtained $\tilde{I}_\alpha = 0.034$, $\tilde{I}_\beta = 0.0032$, $\tilde{\tau}_\alpha = 25.74\text{ }\mu\text{m}$, and $\tilde{\tau}_\beta = 37.19\text{ }\mu\text{m}$. The effect of the passive materials on the calculation of angular distribution of photons reaching the active volume was found to be negligible for this analysis. The active area of the ^{55}Fe was used in the simulations.

A. Results for CCD-A

The spectrum of measured charge for CCD-A is shown in the left panel of Fig. 2, and is compared with a detailed

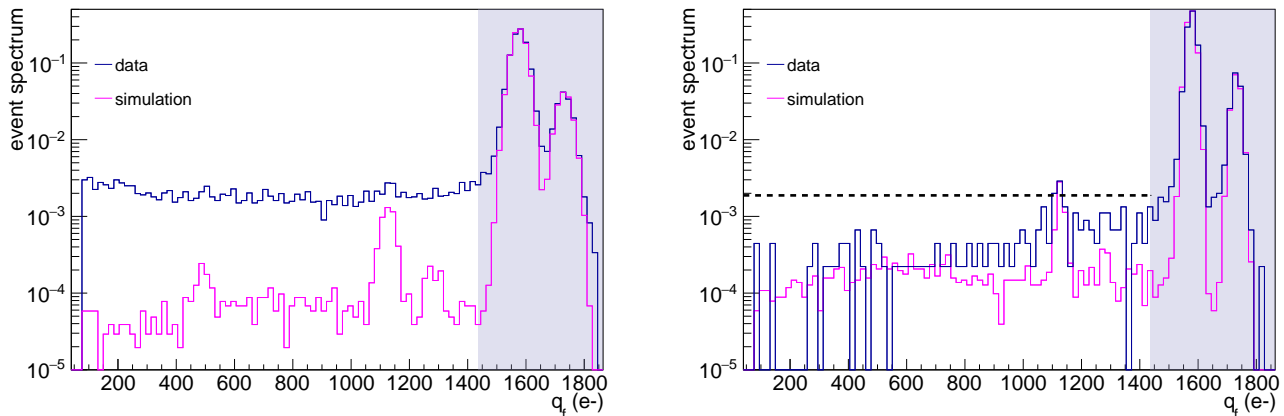


FIG. 2. Event spectra for CCD-A (left) and CCD-B (right) calculated using a bin size of 70 eV normalized by the number of measured events in the K_α peak. Blue: measured spectra. Magenta: Simulated spectra of events from Geant4. Left panel: spectra for CCD-A; 35195 events in the histogram; 26697 events in the K_α peak. Right panel: event spectra for CCD-B; 5452 events in the histogram; 4482 events in the K_α peak. The dashed black line indicates the expected level of events if the partial charge collection layer on CCD-B was same as the one measured on CCD-A.

Geant4 [30] simulation assuming perfect CCE for the entire volume of the sensor ($\varepsilon(z) = 1$). This simulation computes the contribution to the spectrum that comes from multiple scattering events in the dead layer, Compton interactions, and other processes with low probability such as fluorescence. This simulation accounts for the possibility of electrons leaving the CCD and producing a partial energy deposition event. As the direction of the electron is highly correlated with the direction of the incoming X-ray only a small fraction leave the CCD. Our simulation also includes the possibility of keV-scale photons to leave the sensor producing an event with reduced reconstructed energy. The Geant4 simulation geometry includes all accessories and support materials (including the vacuum vessel walls) that have a direct line of sight to the active area of the source. The source model includes the Ni backing material, the 1 μm active foil and the 0.25 mm Be window. The layers shown in Fig. 1 were also included in the back side of the sensor. We also modeled the copper plates that are part of the sensor's package. We did not include the stainless steel screws (used to hold the copper package in place) nor the flex cable that connects the sensor to the readout electronics. Their contribution is expected to be negligible as there is no direct line of sight between them and the sensor. For the comparison of the simulated spectrum with the measured one we include the Fano fluctuations [27] and the readout noise added in quadrature. The environmental background was measured to be below 2×10^{-5} in the scale of Fig. 2 and has a negligible contribution. The K_α and K_β peaks from Table I are evident. The excess of reconstructed events to the left of these peaks is attributed to the PCC layer, where charge recombination produces a measurement below the peak energy. The bumps in the simulation around 1100 e^- and 1300 e^- are the K_α and

K_β escape peaks, respectively, as discussed in Ref.[31]. These peaks are expected to be suppressed in the measured data because escape events are produced when a Si-fluorescence photon created in the interaction leaves the detector without being recorded. As the attenuation length in silicon for Si-fluorescence photons is $\sim 10 \mu\text{m}$, these escape events need to occur close to the surface of the sensor for the low-energy photons to have a large probability of leaving the detector. This region is the most affected by the energy-smearing effect produced by the PCC layer. Once the PCC is fully characterized, using the method described in this work, it is trivial to use the 3D tracking information produced by the G4 simulation to compute a simulated spectrum that includes the effect of the PCC layer (we used this technique as a self consistency check). The peak at $\sim 500 e^-$ in the simulated spectrum is produced by silicon fluorescence in the SiO_2 dead layer that covers the backside of the CCD. This peak is not expected to be visible in the measured spectrum because most of the low energy Si-fluorescence photons produced in the SiO_2 dead layer interact in the PCC layer before they can reach the region of full charge collection.

The data shown in Fig. 2 is used to measure the CCE function $\varepsilon(z)$ following the prescription in Section II B, and the results are shown in Fig. 3. The depth scale is chosen such that $\varepsilon(z = 0) = 0.9$. The shaded region corresponds to the energies between 5.4 keV and 7 keV where the events from K_α and K_β are dominant and systematic uncertainties are expected to be important. In this region the precise shape of ε curve is less reliable.

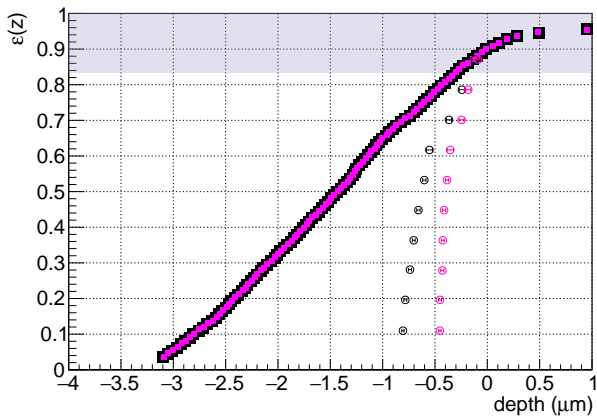


FIG. 3. Measured charge collection efficiency for a CCD-A (solid square markers) and CCD-B (open circle markers). The black points show the results without considering the background events predicted by the simulation. The magenta point show the results after correcting the experimental spectra by subtracting the background events from the simulations. The shaded area indicates the region where the detailed shape of the X-ray peaks affects the measurement introducing more uncertainty.

B. Results for CCD-B

The spectrum of measured charge for CCD-B is shown in the right panel of Fig. 2, and compared with a detailed Geant4 simulation assuming perfect CCE. This simulation includes the contribution to the spectrum that comes from multiple scattering events in the dead anti-reflective layer, Compton interactions, and other processes with low probability such as fluorescence. In contrast to the results for CCD-A, the simulated spectrum of CCD-B can account for a significant fraction of the low energy events and may play a role in the characterization of the PCC layer. For this reason we compared results from using Penelope or Livermore electromagnetic models included in Geant4 and obtained statistically compatible simulated spectra. Although we recognize that there may be additional contributions to the low energy spectrum, they would only reduce the number of candidate events produced in the PCC layer and thus further reduce the thickness of the PCC layer. To study this systematic we are planning an experiment using lower energy photons that will allow for a better precision on the measurement of thin PCC layers due to their smaller attenuation length.

As with CCD-A, the K_α and K_β spectral lines are evident, CCD-B has a different output stage that allows for a lower noise readout and produces higher resolution peaks [6]. The relative rate of events on the left of the peaks is well below the rate observed for CCD-A and consistent with the simulation. These events are produced mostly by low probability Compton scattering of X-rays. The environmental background for this CCD was below 1×10^{-7} in the scale of Fig. 2 and can be safely ignored

for this analysis. The CCE function $\varepsilon(z)$ is determined as discussed in Section II B and the results are shown in Fig. 3. The measurement of $\varepsilon(z)$ is also performed after subtracting the predicted background from the Geant4 simulation. As before, the horizontal axis is selected such that $\varepsilon(z = 0) = 0.9$.

IV. CONCLUSIONS

The results of CCD-A and CCD-B showed in Fig. 3 demonstrate the large impact that the backside processing has in the CCE for back-illuminated detectors. When a layer of a few microns with charge recombination is present on the CCD, the spectrum for low energy X-rays gets significantly distorted. The charge recombination generates a significant number of lower energy events in the spectrum. The backside processing performed in detectors optimized for astronomical instruments eliminates this issue for the most part, as shown with CCD-B. The backside treatment from CCD-B can be applied to thicker detectors. We plan to explore other techniques as in [32, 33]. The generation of low energy events constitute a major concern for experiments looking for rare signals near the detector threshold [1–7, 10, 11].

In this work we introduced a technique to characterize the CCE in back-illuminated CCDs that can easily be generalized to other semiconductor detectors. The technique uses tools that are commonly available at detector characterization laboratories. As shown here, the method is capable of measuring a PCC layer of a few micrometers even when a dead layer is present. The sensitivity to much thinner PCC layers is only limited by the energy of the ^{55}Fe X-rays used. The technique can be easily extended for the measurement of much thinner recombination layers using lower-energy X-rays. This technique is a powerful tool in the optimization of detectors for the next generation of low threshold experiments looking for rare events such as dark matter, or coherent neutrino-nucleus scattering [8, 9, 12]. This method can also be used for the characterization of back-illuminated CCD sensors used in space-based X-ray observatories such as Hitomi [13–15] or the upcoming XRISM [16].

The contribution of the PCC layer to low energy events depends on the nature of the interacting background particle. Particles with penetration range similar to the PCC layer thickness produce larger contribution. Last results from DAMIC (Dark Matter in CCDs) experiment [34] show that a significant portion of the low energy events comes from this region and they can be eliminated if the layer is narrowed.

ACKNOWLEDGMENTS

We thank the SiDet team at Fermilab for the support on the operations of CCDs and Skipper-CCDs, especially Kevin Kuk and Andrew Lathrop. This work was

supported by Fermilab under DOE Contract No. DE-AC02-07CH11359. This manuscript has been authored by Fermi Research Alliance, LLC under Contract No. DE-AC02-07CH11359 with the U.S. Department of Energy, Office of Science, Office of High Energy Physics. The CCD development work was supported in part by the Director, Office of Science, of the U.S. Department of Energy under No. DE-AC02-05CH11231. The United States Government retains and the publisher, by accepting the article for publication, acknowledges that the United States Government retains a non-exclusive, paid-up, irrevocable, worldwide license to publish or reproduce the published form of this manuscript, or allow others to do so, for United States Government purposes.

APPENDIX: DETAILS OF THE METHOD

The details of the method to measure the CCE in the backside of a back-illuminated CCD are presented in Table II. The details of the method used with the ^{55}Fe source having two X-ray lines are presented in Table III.

-
- 1) Calculate angular distribution of incident photons**
Based on the geometry of the experiment evaluate angle distribution of incident photons reaching the region of interest in the sensor, $h(\theta)$.

 - 2) Calculate the depth distribution of events**
Calculate $g'(z, \theta) = \exp(-z/(\lambda \cos(\theta)))h(\theta)/(\cos(\theta)\lambda)$, $z > 0$. Integrate this distribution over all possible values of θ to find the marginal *pdf* of the interaction depths $g(z)$ (follow Eq. 1). Then, find its *cdf* $G(z)$ (you can follow Eq. 3).

 - 3) Make an spectrum of measured events**
Calculate the spectrum of events reconstructed from the data and normalize it by total number of events (N_T). This is the estimation $f(q_f)$.

 - 4) Calculate the *cdf* of the measured spectrum of events, $F(q_f)$.**
Use Eq. 3.

 - 5) Find z**
For a particular charge value q_f , find z that equals $F(q_f) = G(z)$. This step can also be applied using the the complement of the *cdf* to avoid systematic errors from noise models.

 - 6) Calculate the efficiency at z**
 $\varepsilon(z) = q_f/q_i$

 - 7) Repeat steps 4, 5 and 6 for a different q_f to complete $\varepsilon(z)$.**
-

TABLE II. Methodology to calculate the PCC efficiency function using a monochromatic X-ray source.

-
- [1] A. Aguilar-Arevalo, D. Amidei, X. Bertou, M. Butner, G. Canelo, A. Casta~neda Vázquez, B. A. Cervantes Vergara, A. E. Chavarria, C. R. Chavez, J. R. T. de Mello Neto, et al. (DAMIC), “Search for low-mass WIMPs in a 0.6 kg day exposure of the DAMIC experiment at SNOLAB,” *Phys. Rev. D* **94**, 082006 (2016), arXiv:1607.07410 [astro-ph.CO].
 - [2] A. Aguilar-Arevalo et al. (DAMIC), “First Direct-Detection Constraints on eV-Scale Hidden-Photon Dark Matter with DAMIC at SNOLAB,” *Phys. Rev. Lett.* **118**, 141803 (2017), arXiv:1611.03066 [astro-ph.CO].
 - [3] A. Aguilar-Arevalo et al. (DAMIC), “Constraints on Light Dark Matter Particles Interacting with Electrons from DAMIC at SNOLAB,” *Phys. Rev. Lett.* **123**, 181802 (2019), arXiv:1907.12628 [astro-ph.CO].
 - [4] M. Crisler, R. Essig, J. Estrada, G. Fernandez, J. Tiffenberg, M. Sofo haro, T. Volansky, and T.-T. Yu (SENSEI), “SENSEI: First Direct-Detection Constraints on sub-GeV Dark Matter from a Surface Run,” *Phys. Rev. Lett.* **121**, 061803 (2018), arXiv:1804.00088 [hep-ex].
 - [5] O. Abramoff et al. (SENSEI), “SENSEI: Direct-Detection Constraints on Sub-GeV Dark Matter from a Shallow Underground Run Using a Prototype Skipper-CCD,” *Phys. Rev. Lett.* **122**, 161801 (2019), arXiv:1901.10478 [hep-ex].
 - [6] J. Tiffenberg, M. Sofo-Haro, A. Drlica-Wagner, R. Essig, Y. Guardincerri, S. Holland, T. Volansky, and T.-T. Yu, “Single-electron and single-photon sensitivity with a silicon Skipper CCD,” *Phys. Rev. Lett.* **119**, 131802 (2017), arXiv:1706.00028 [physics.ins-det].
 - [7] L. Barak, I. M. Bloch, M. Cababie, G. Canelo, L. Chaplinsky, F. Chierchie, M. Crisler, A. Drlica-Wagner, R. Essig, J. Estrada, et al., “SENSEI: Direct-Detection Results on sub-GeV Dark Matter from a New Skipper-CCD,” arXiv e-prints, arXiv:2004.11378 (2020), arXiv:2004.11378 [astro-ph.CO].
 - [8] M. Settimo, “Search for low-mass dark matter with the DAMIC experiment,” arXiv e-prints, arXiv:2003.09497 (2020), arXiv:2003.09497 [hep-ex].
 - [9] The Oscura project is an R&D effort supported by Department of Energy to develop 10 kg skipper-CCD dark matter search.
 - [10] A. Aguilar-Arevalo, X. Bertou, C. Bonifazi, G. Canelo, A. Casta~neda, B. Cervantes Vergara, C. Chavez, J. C. D’Olivo, J. C. Dos Anjos, J. Estrada, et al. (CONNIE Collaboration), “Exploring low-energy neutrino physics with the coherent neutrino nucleus interaction experiment,” *Phys. Rev. D* **100**, 092005 (2019).
 - [11] CONNIE Collaboration, A. Aguilar-Arevalo, X. Bertou, C. Bonifazi, G. Canelo, B. A. Cervantes-Vergara, C. Chavez, J. C. D’Olivo, J. C. Dos Anjos, J. Estrada, et al., “Search for light mediators in the low-energy data of the CONNIE reactor neutrino experiment,” *Journal of High Energy Physics* **2020**, 54 (2020), arXiv:1910.04951 [hep-ex].
 - [12] The Violeta Collaboration is planning a kg-scale Skipper-CCD experiment at a nuclear reactor facility.
 - [13] T. Takahashi, M. Kokubun, K. Mitsuda, R. L. Kelley, T. Ohashi, F. Aharonian, H. Akamatsu, F. Akimoto, S. W. Allen, N. Anabuki, et al., “Hitomi (ASTRO-H) X-

1) Calculate angular distribution of incident photons
Based on the geometry of the experiment evaluate angle distribution of incident photons reaching the region of interest in the sensor, $h(\theta)$.
2) Calculate the depth distribution of events
Calculate $g'_\alpha(z, \theta)$ and $g'_\beta(z, \theta)$ for $z > 0$ from Eq. 5 and 6, respectively. Integrate these distributions over all possible values of θ to find the marginal distributions of the interaction depths $g_\alpha(z)$ and $g_\beta(z)$ (follow Eq. 1). Then, find their <i>cdf</i> $G_\alpha(z)$ and $G_\beta(z)$ (you can follow Eq. 3). Calculate the final <i>cdf</i> of the interaction depth $G(z) = p_\alpha G_\alpha(z) + p_\beta G_\beta(z)$.
3) Make an spectrum of measured events
Calculate the spectrum of events reconstructed from the data and normalize it by total number of events (N_T). This is the estimation $f(q_f)$.
4) Calculate the <i>cdf</i> of the measured spectrum of events, $F(q_f)$.
Use Eq. 3.
5) Find z
For a particular charge value q_f , find z that equals $F(q_f) = G(z)$. This step can also be applied using the the complement of the <i>cdf</i> to avoid systematic errors from noise models.
6) Calculate the efficiency at z
$\varepsilon(z) = q_f / (p_\alpha q_{i,\alpha} + p_\beta q_{i,\beta})$
7) Repeat steps 4, 5 and 6 for a different q_f to complete $\varepsilon(z)$.

TABLE III. Methodology to calculate the partial charge collection efficiency function using an ^{55}Fe source.

- ray Astronomy Satellite,” *Journal of Astronomical Telescopes, Instruments, and Systems* **4**, 021402 (2018).
- [14] M. J. L. Turner, A. Abbey, M. Arnaud, M. Balasini, M. Barbera, E. Belsole, P. J. Bennie, J. P. Bernard, G. F. Bignami, M. Boer, et al., “*The European Photon Imaging Camera on XMM-Newton: The MOS cameras*,” *Astronomy and Astrophysics* **365**, L27 (2001), arXiv:astro-ph/0011498 [astro-ph].
- [15] K. Koyama, H. Tsunemi, T. Dotani, M. W. Bautz, K. Hayashida, T. G. Tsuru, H. Matsumoto, Y. Ogawara, G. R. Ricker, J. Doty, et al., “*X-Ray Imaging Spectrometer (XIS) on Board Suzaku*,” *Publications of the Astronomical Society of Japan* **59**, 23 (2007).
- [16] XRISM Science Team, “*Science with the X-ray Imaging and Spectroscopy Mission (XRISM)*,” arXiv e-prints, arXiv:2003.04962 (2020), arXiv:2003.04962 [astro-ph.HE].
- [17] T. Hatsui and H. Graafsma, “*X-ray imaging detectors for synchrotron and xfel sources*,” *IUCrJ* **2** (2015), 10.1107/S205225251500010X.
- [18] G. Cencelo, C. Chavez, F. Chierchie, J. Estrada, G. Fernandez Moroni, E. E. Paolini, M. Sofo Haro, A. Soto, L. Stefanazzi, J. Tiffenberg, et al., “*Low Threshold Acquisition controller for Skipper CCDs*,” arXiv e-prints, arXiv:2004.07599 (2020), arXiv:2004.07599 [astro-ph.IM].
- [19] M. Sofo Haro, G. Fernandez Moroni, and J. Tiffenberg, “*Studies on small charge packet transport in high-resistivity fully-depleted CCDs*,” arXiv e-prints, arXiv:1906.11379 (2019), arXiv:1906.11379 [physics.ins-det].
- [20] S. E. Holland, D. E. Groom, N. P. Palaio, R. J. Stover, and M. Wei, “*Fully depleted, back-illuminated charge-coupled devices fabricated on high-resistivity silicon*,” *IEEE Transactions on Electron Devices* **50**, 225 (2003).
- [21] J. R. Janesick, *Scientific charge-coupled devices*, Vol. 83 (SPIE press, 2001).
- [22] J. A. del Alamo and R. M. Swanson, “*Modelling of minority-carrier transport in heavily doped silicon emitters*,” *Solid-State Electronics* **30**, 1127 (1987).
- [23] S. Nikzad, M. E. Hoenk, P. J. Grunthaner, R. W. Terhune, F. J. Grunthaner, R. Winzenread, M. M. Fattahi, H.-F. Tseng, and M. P. Lesser, in *Proceedings of the SPIE*, Society of Photo-Optical Instrumentation Engineers (SPIE) Conference Series, Vol. 2198, edited by D. L. Crawford and E. R. Craine (1994) pp. 907–915.
- [24] E. T. Hamden, A. D. Jewell, C. A. Shapiro, S. R. Cheng, T. M. Goodsall, J. Hennessy, M. Hoenk, T. Jones, S. Gordon, H. R. Ong, et al., “*Charge-coupled devices detectors with high quantum efficiency at UV wavelengths*,” *Journal of Astronomical Telescopes, Instruments, and Systems* **2**, 036003 (2016), arXiv:1701.02733 [astro-ph.IM].
- [25] C. J. Bebek, J. H. Emes, D. E. Groom, S. Haque, S. E. Holland, P. N. Jelinsky, A. Karcher, W. F. Kolbe, J. S. Lee, N. P. Palaio, et al., “*Status of the CCD development for the Dark Energy Spectroscopic Instrument*,” *Journal of Instrumentation* **12**, C04018 (2017).
- [26] M. H. Fabricius, C. J. Bebek, D. E. Groom, A. Karcher, and N. A. Roe, in *Proceedings of the SPIE*, Society of Photo-Optical Instrumentation Engineers (SPIE) Conference Series, Vol. 6068, edited by M. M. Blouke (2006) pp. 144–154.
- [27] D. Rodrigues, K. Andersson, M. Cababie, A. Donadon, A. Botti, G. Cencelo, J. Estrada, G. Fernandez-Moroni, R. Piegaia, M. Senger, et al., “*Absolute measurement of the Fano factor using a Skipper-CCD*,” arXiv e-prints, arXiv:2004.11499 (2020), arXiv:2004.11499 [physics.ins-det].
- [28] M.-M. Bé, V. Chisté, C. Dulieu, E. Browne, C. Baglin, V. Chechev, N. Kuzmenko, R. Helmer, F. Kondev, D. MacMahon, et al., *Table of Radionuclides*, Monographie BIPM-5, Vol. 3 (Bureau International des Poids et Mesures, Pavillon de Breteuil, F-92310 Sèvres, France, 2006).
- [29] <https://engineering.lbl.gov/microsystems-laboratory/>.
- [30] <https://geant4.web.cern.ch>.
- [31] J. Jaeckel and S. Roy, “*Spectroscopy as a test of Coulomb’s law: A Probe of the hidden sector*,” *Phys. Rev. D* **82**, 125020 (2010), arXiv:1008.3536 [hep-ph].
- [32] Q. Looker, B. Aguirre, M. Hoenk, A. Jewell, M. Sanchez, and B. Tierney, “*Superlattice-enhanced silicon soft x-ray and charged particle detectors with nanosecond time response*,” *Nuclear Instruments and Methods in Physics Research Section A: Accelerators, Spectrometers, Detectors and Associated Equipment* **916**, 148 (2019).
- [33] J. Blacksborg, S. Nikzad, M. E. Hoenk, S. E. Holland, and W. F. Kolbe, “*Near-100silicon imagers*,” *IEEE Transactions on Electron Devices* **55**, 3402 (2008).
- [34] R. Catena and P. Ullio, “*Results on low-mass weakly interacting massive particles from a 11 kg-day target exposure of damic at snolab*,” (2020), arXiv:2007.15622 [astro-ph.CO].